POLITECNICO DI TORINO
Repository ISTITUZIONALE

Set of Boundary Conditions for Aerodynamic Design

Original
Set of Boundary Conditions for Aerodynamic Design / Ferlauto, Michele; Iollo, Angelo; Zannetti, Luca. - In: AIAA JOURNAL. - ISSN 0001-1452. - 42:8(2004), pp. 1582-1592. [10.2514/1.2340]

Availability:
This version is available at: 11583/1407274 since:

Publisher:
American Institute of Aeronautics and Astronautics 1801 Alexander Bell Drive, Suite 500 Reston, VA

Published
DOI:10.2514/1.2340

Terms of use:

This article is made available under terms and conditions as specified in the corresponding bibliographic description in the repository

Publisher copyright

(Article begins on next page)

12 October 2024

AIAA JOURNAL
Vol. 42, No. 8, August 2004

Set of Boundary Conditions for Aerodynamic Design

M. Ferlauto,* A. Iollo,† and L. Zannetti‡
Politecnico di Torino, 10129 Turin, Italy

Robust and flexible numerical methodologies for the imposition of boundary conditions are required to formulate well-posed problems. A boundary condition should be nonreflecting, to avoid spurious perturbations that can provocate unsteadiness or instabilities. The reflectiveness of various boundary conditions is analyzed in the context of the Godunov methods. A nonlinear, isentropic wave propagation model is used to investigate the reflection mechanism on the flowfield borders, and a parameter τ is defined to give a measure of the boundary reflectiveness. A new set of boundary conditions, in which $\tau = 0$, that is, totally nonreflecting, is then proposed. The approach has been integrated in an aerodynamic design procedure using a distributed boundary control.

Nomenclature

$\boldsymbol{A}, \boldsymbol{B}$	=	vector of convective fluxes
$\boldsymbol{A}_U, \boldsymbol{B}_U$	=	Jacobians of vectors $\boldsymbol{A}, \boldsymbol{B}$
e	=	total internal energy per unit of volume
$\boldsymbol{i}, \boldsymbol{\eta}, \boldsymbol{k}$	=	unit vectors
L_{ref}	=	reference length
M	=	Mach number
$\boldsymbol{n}$	=	normal unit vector
p	=	pressure
$\boldsymbol{Q}$	=	vector of source terms
R_1, R_2, R_3	=	Riemann invariants pertinent to the characteristic lines of slopes $u - a$, u, and $u + a$, respectively
S	=	entropy
T^0	=	total temperature
t	=	time
$\boldsymbol{U}$	=	vector of conservative variables
u, v, w	=	velocity components in the cylindrical frame of reference
γ	=	ratio of specific heats
Δ	=	difference
Γ_b	=	boundary of Ω_b
$\boldsymbol{\Lambda}$	=	vector of lagrangian multipliers λ_i
$\lambda_i, \mu, \xi_i, \xi_o$	=	Lagrangian multipliers
ρ	=	density
Ω	=	domain in $(x, r) \in R^2$ on the meridional plane
Ω_b	=	projection of the blade surface onto the meridional plane

Subscripts

b	=	blade
i	=	inlet
l	=	leading edge
o	=	outlet
ref	=	reference value
t	=	trailing edge
∞	=	freestream

Superscripts

$*$	=	value at the boundary interface
$-$	=	target value

Introduction

FUTURE developments of inverse design will concentrate on enhancements of the enforcement of boundary conditions, to be able to increase the robustness of numerical procedures and to formulate well-posed problems. Virtual boundaries are frequently used in the practice of computational fluid dynamics (CFD) to limit the computational domain. These boundaries play a major role in the numerical accuracy of the flowfield solution. The global accuracy of the computation depends on the accuracy of the boundary treatment and on the absence of unphysical, spurious reflections. In external flow computations, for example, the presence of such reflections can be observed when the boundary that simulates asymptotic flowfield conditions is too close to the body or when extrapolation formulas are used to determine the flow variable at the boundary contour. In this context, the use of nonreflecting boundary models is quite attractive: When unphysical reflections are avoided, the computed solution becomes independent of the distance of the far-field boundaries, and a smaller computational domain can be adopted, so that the computational resources can be used to increase the grid resolution. This route has been exploited by many researchers, starting from the theoretical studies on the well posedness of an initial boundary value problem for hyperbolic systems by Kreiss,[1] and the work on absorbing boundary conditions for the numerical simulation of waves by Engquist and Majda.[2] Research was then focused on the numerical modelization of nonreflecting boundary conditions for both Euler and Navier–Stokes equations. For a review see, for example, Refs. 3–5 and references therein. Let us consider how a boundary condition reflects the signals that come from the interior domain. In general, a new perturbation, which can be stronger or weaker than the incident wave, arises at the boundary. For the simulations of systems overrelaxed to the steady state, such reflections are problematic. Because one is in fact interested in the steady flowfield solution, any undamped perturbation is, at least, CPU time consuming, and convergence is delayed. Special care must be adopted in imposing boundary conditions when solving inverse problems, not only for convergence problems but also as well-posedness requirements are concerned.[6–8] For internal flows, the strong coupling between inner flowfield and boundary conditions does not allow the straightforward application of numerical techniques valid for external flows. For instance, the use of Riemann invariant boundary conditions (or their linearized equivalent) is a standard technique in external aerodynamic computations, where the value of the invariants can be set from the freestream conditions. For turbomachinery flow calculations, however, the value of Riemann invariant that matches the desired operating conditions cannot be set a priori, and it should be found iteratively.

Received 9 May 2003; revision received 13 January 2004; accepted for publication 5 February 2004. Copyright © 2004 by the American Institute of Aeronautics and Astronautics, Inc. All rights reserved. Copies of this paper may be made for personal or internal use, on condition that the copier pay the $10.00 per-copy fee to the Copyright Clearance Center, Inc., 222 Rosewood Drive, Danvers, MA 01923; include the code 0001-1452/04 $10.00 in correspondence with the CCC.

*Research Associate, Aerospace Engineering Department, Corso Duca degli Abruzzi 24,10129; michele.ferlauto@polito.it.

†Assistant Professor, Aerospace Engineering Department, Corso Duca degli Abruzzi 24,10129; angelo.iollo@polito.it.

‡Professor, Aerospace Engineering Department, Corso Duca degli Abruzzi 24,10129; luca.zannetti@polito.it.

The present work was initially motivated as an attempt to overcome some practical limitations that the use of conventional boundary conditions could have on inverse design. The reflection properties of standard boundary conditions could result to be problematic or infeasible when dealing with inverse CFD methods, especially for turbomachinery design problems. In the first part of the paper the reflecting/nonreflecting properties of some boundary conditions that are usually used in CFD are analyzed. The interaction of acoustic perturbations with the boundary is modeled using a characteristic wave approach. A parameter τ is derived from the model to measure the reflectiveness of a boundary condition. Some limits that arise with the use of conventional boundary conditions in aerodynamic design are discussed. A different approach to boundary condition enforcement is investigated in the second part of the paper. In the context of a methodology for the optimal design of turbomachinery,[9] a class of nonreflecting boundary conditions is presented, derived in the framework of a distributed boundary control based on the adjoint of the governing equations. The Riemann invariants are taken as boundary controls, and a functional that represents the convergence to the given boundary conditions is defined. Totally nonreflecting boundaries are obtained by minimizing this functional with respect to the controls; nevertheless, the prescribed physical conditions are ensured. Finally, the performances and accuracy of the new procedure were investigated in several numerical tests, and the results were then compared with the performance that can be obtained using conventional boundary conditions.

Boundary Condition Reflectiveness

The reflectiveness of typical boundary conditions is analyzed in this section. On this subject, the interested reader can find an exhaustive eigenmode analysis, for example, by Darmofal et al.[10]

When compressible flows are dealt with, it is natural to work with characteristic variables,[3] which also give a straightforward physical interpretation to the analysis. Whenever a characteristic, approaching the boundary, is not in agreement with the imposed boundary conditions, it reflects on the interior, giving rise to a new perturbation that travels backward into the flow. This reflection is governed by the coupling of the boundary condition with the traveling signal. In a one-dimensional, isentropic model, the set of boundary conditions can be represented by the functional form

$$\mathcal{B}[a^*(\boldsymbol{U}), u^*(\boldsymbol{U})] = 0 \tag{1}$$

where a is the sound velocity, u the flow velocity, and $\boldsymbol{U}$ the conservative variables as defined in Eq. (21). According to Ref. 11, the signals, or Riemann invariants, conveyed along the characteristics are approximated by

$$R_1 = a/\kappa - u, \qquad R_2 = s, \qquad R_3 = a/\kappa + u \tag{2}$$

where $\kappa = (\gamma - 1)/2$ and s is entropy. R_2 expresses the convection of the entropy along the characteristic lines of slope u. These expressions for the Riemann invariants are derived by neglecting the entropy contributions to R_1 and R_3, otherwise no one invariant can be defined because entropy depends on the thermodynamic history of flow particles. This assumption has been widely investigated in the derivation of nonlinear, approximate Riemann solvers (see Refs. 11 and 12), and it has proved to give good approximations for a wide range of Mach numbers. Although the wave propagation is governed by the linear system (2), the reflection mechanism requires the coupling with relation (1) and results in a nonlinear combination of the flow variables.

Now, let us suppose that R_3, the signal that propagates along the characteristic lines of slope $u + a$, is the signal that approaches the boundary. Then, according to the theory of hyperbolic systems, the reflected signal will travel as R_1 because it belongs to the family of characteristic lines with slope $u - a$. A measure of the relative strength of the new perturbation is given by

$$\delta R_1 = \frac{\partial R_1}{\partial R_3}\delta R_3 = \tau \delta R_3 \tag{3}$$

The derivative $\tau = \partial R_1/\partial R_3$ here plays the role of an amplification or damping factor. If the coupling of Eqs. (1) and (2) results in values of $|\tau| < 1$, the boundary condition is able to reduce the initial gap between the flow state and the incoming signal. For values of $|\tau| > 1$, the perturbation is somehow amplified by the boundary condition. When $|\tau| = 1$, the perturbation is reflected exactly. Low values of τ are advantageous because they enhance the overall convergence by damping any perturbation that eventually arises during the computation of the unsteady flow. In spite of its simplicity, the reduced-order model of the wave system propagation here proposed is a basic representation of nonlinear wave interactions,[11,12] and it retains most of its effectiveness even for two- or three-dimensional configurations. The theoretical results concerning the reflectiveness of several boundary conditions, obtained by using the discussed wave propagation model, are detailed in the following sections.

Wall Boundary

At solid boundaries that move in a general manner, the wall impermeability is ensured by fixing the normal component of flow velocity V_n,

$$\mathcal{B}(a, u, \boldsymbol{U}) = u^* - V_n = 0 \tag{4}$$

When system (2) is recalled, the sound and flow velocities in boundary condition (4) can be expressed in terms of R_1 and R_3:

$$a^* = \kappa(R_3 + R_1)/2, \qquad u^* = (R_3 - R_1)/2 \tag{5}$$

By differentiating the boundary condition (4), we obtain

$$\delta\mathcal{B} = \delta R_3 - \delta R_1 = 0 \tag{6}$$

and the parameter τ can be defined as

$$\tau = \frac{\partial R_3}{\partial R_1} = 1 \tag{7}$$

which is a constant. From Eq. (7), the wall boundary condition reflects exactly an incident perturbation.

Inlet Boundary

The inlet flow can be either subsonic or supersonic. In the latter case, reflection is impossible because none of the signals can flow back to the inlet and all of the flow variables must be given. In one dimension, the total temperature, the entropy (or the total pressure), and the inlet Mach number are usually assigned. A supersonic inlet is already a nonreflecting surface in the conventional boundary treatment.

When the inlet flow is subsonic, the total temperature and entropy are imposed. The reflection mechanism is governed by the condition on the total temperature because the second boundary condition (BC) just fixes the entropy level at the inlet. In this case, the Riemann invariant $R_1 = R_1^*$ comes from the interior domain (Fig. 1b) and does not depend on the BC. The total temperature is imposed through the BC

$$\mathcal{B}(a, u, \boldsymbol{U}) = a^2 + \kappa u^2 - \gamma T^0 = 0 \tag{8}$$

whereas sound and flow velocities can be expressed in terms of R_1 and R_3 by Eqs. (5). The differential of the BC is

$$\delta\mathcal{B} = [\kappa(R_3 + R_1) + (R_3 - R_1)]\delta R_3 + [\kappa(R_3 + R_1) - (R_3 - R_1)]\delta R_1 = 0 \tag{9}$$

that is,

$$\tau = \frac{\partial R_3}{\partial R_1} = \frac{1-\kappa}{1+\kappa} - \frac{2\kappa}{1+\kappa}\frac{1/\kappa - M}{\sqrt{[(1+\kappa)/\kappa](1+\kappa M^2) - \kappa(1/\kappa - M)}} \tag{10}$$

The τ function is plotted vs the Mach number in Fig. 1. We observe that is $\tau < 1$ and the damping effect increases as the Mach number increases from $0 < M < 1$.

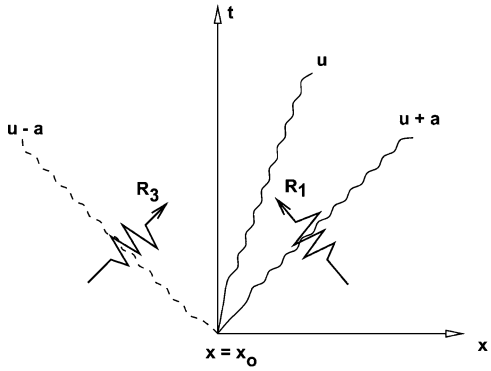

Fig. 1a Typical wave pattern of the Riemann problem (see Ref. 11) for a subsonic inlet.

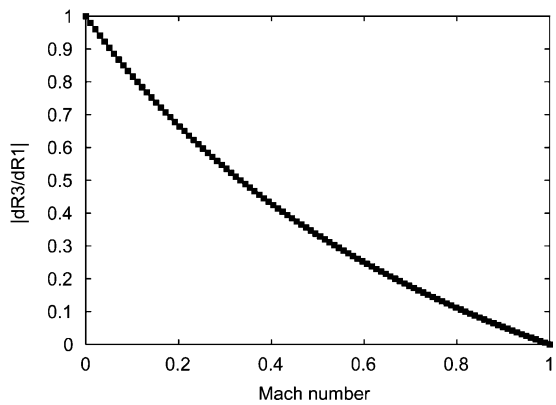

Fig. 1b Inlet reflectiveness τ vs Mach number.

Outlet Boundary

As for the inlet, one has to distinguish whether the flow is subsonic or supersonic. When the flow is supersonic, all of the flow variables are extrapolated from the interior domain and no BC is required, according to the theory of hyperbolic systems. The supersonic outlet is, therefore, a nonreflecting boundary surface. When the outlet flow is subsonic, one BC must be prescribed. In general, the static pressure level p_{ex} is imposed. The sound velocity at the outlet can be expressed as

$$a^* = a_{\mathrm{ex}} = \sqrt{\gamma p_{\mathrm{ex}}^{(\gamma-1)/\gamma}} \tag{11}$$

Therefore, the BC is

$$\mathcal{B}(a, u, \boldsymbol{U}) = a^* - \sqrt{\gamma p_{\mathrm{ex}}^{(\gamma-1)/\gamma}} = 0 \tag{12}$$

and, from Eq. (5),

$$\kappa(R_3 + R_1)/2 - \sqrt{\gamma p_{\mathrm{ex}}^{(\gamma-1)/\gamma}} = 0 \tag{13}$$

By differentiation, this leads to

$$\delta R_3 + \delta R_1 = 0, \qquad \tau = \frac{\partial R_1}{\partial R_3} = -1 \tag{14}$$

so that an incidence perturbation is reflected exactly. The static pressure is not the only variable that can be adopted. For example, it has been demonstrated that an ill-posedness problem in blade design using inverse formulations can be overcome by fixing the mass flow at the cascade exit in certain way.[7] One can, for instance, set the axial Mach number M_{ex} at the outlet. In this case $u^* = a^* M_{\mathrm{ex}}$ and

$$\mathcal{B}(a, u, \boldsymbol{U}) = u^* - a^* M_{\mathrm{ex}} = 0 \tag{15}$$

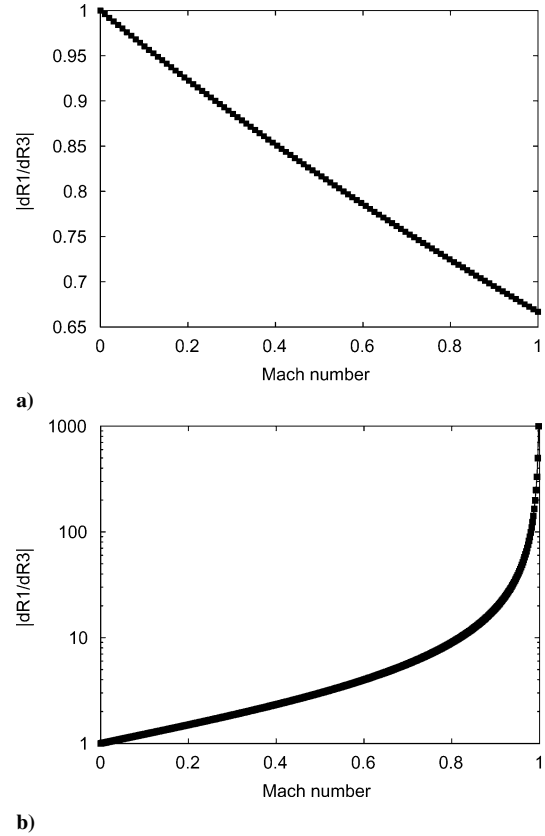

Fig. 2 Outlet reflectiveness τ vs Mach number: a) axial Mach number prescribed as BC and b) mass flow rate imposed at exit.

and the expressions of the differential and τ are

$$\delta\mathcal{B} = (1 - \kappa M_{\mathrm{ex}})\delta R_3 - (1 + \kappa M_{\mathrm{ex}})\delta R_1 = 0$$

$$\tau = \frac{\partial R_1}{\partial R_3} = \frac{(1 - \kappa M_{\mathrm{ex}})}{(1 + \kappa M_{\mathrm{ex}})} \tag{16}$$

Another possibility is to set the mass flow rate $\dot{m} = (\rho u)^*$, which is often a main design parameter. As can be seen, the straight imposition of the mass flow results in a strong reflective BC. By reformulating the density as a function of the sound velocity and by using system (2), from $d\dot{m} = 0$ we obtain

$$\mathcal{B}(a, u, \boldsymbol{U}) = \gamma^{-1/(\gamma-1)} a^{*1/\kappa} u^* - (\rho u)_{\mathrm{ex}} = 0 \tag{17}$$

and the differential $\delta\mathcal{B}$ is

$$\delta\mathcal{B} = [(R_3 - R_1)/\kappa + (R_3 - R_1)]\delta R_3 + [(R_3 - R_1)/\kappa - (R_3 - R_1)]\delta R_1 = 0 \tag{18}$$

The amplification factor τ is given by

$$\tau = (1 + M_{\mathrm{ex}})/(1 - M_{\mathrm{ex}}) \tag{19}$$

The τ diagrams from expressions (16) and (19) are shown in Fig. 2. As can be seen, the enforcement of the axial Mach number at the outlet has a slight damping effect, whereas the constraint on the mass flow results in a severe and strong reflecting BC that yields in practice to divergence in the numerical computations.

New Set of BCs

The conventional enforcement of BCs leads to a system of equations that combines the wave propagation model with the physical variable, for example, pressure, total temperature, etc., that has to be prescribed at the boundary, and this often results in a nonlinear coupling of the primitive variables. For transient-to-steady computations, as can be the case of an aerodynamic design, BCs that always result in $\tau = 0$ can be obtained by decoupling the wave propagation

model from the physical conditions that have to be prescribed at the boundary. We propose to set explicitly the value of the Riemann invariant that virtually comes from the border and to update iteratively such a value during the computation to satisfy the physical BC at the steady state. Instead of avoiding reflections by canceling any signal that reenters the flow from the domain border, as the classical approaches to nonreflecting BC do,[3–5] we impose a BC that is independent of the flow at the boundary. In this way the mechanism that leads to reflections is broken. The iterative updating of the Riemann invariants at the border is implemented as an optimization procedure where the Riemann invariants are the control parameters, whereas the physical conditions that have to be enforced at the boundary are rewritten as an objective function that has to be minimized. Regardless of what BCs have to be satisfied, we set both R_3 and R_1. One invariant is imposed according to the flow direction, and the other comes from the domain interior. The flow state at the boundary is given by

$$a^* = \kappa\left(R_1^* + R_3^*\right)/2, \qquad u^* = \left(R_3^* - R_1^*\right)/2 \tag{20}$$

We called this a set of Riemann invariant-based (RIB) BCs. The approach is general and flexible, but requires the availability of a minimization procedure for a fast convergence to the functional extremum, that is, to satisfy the physical constraints at the boundary. Nonreflectiveness of the boundaries is obtained at the cost of an optimization problem. The advantages of adopting the proposed strategy to solve direct problems are dubious. The additional cost should instead be minimal for optimal design procedures[9] that already have to solve an optimization problem. The full computational cost of RIB BC can be motivated by the severe well-posedness requirements of the numerical solution of certain inverse problems.

Mathematical Model

In this part of the paper, details are given on how the proposed boundary conditions can be integrated in the framework of an existing tool for optimal design that combines a flow solver with an optimization procedure.[9,13,14] The flow solver belongs to the through-flow model class, and it is explained in detail in Ref. 15. Briefly, the mathematical model for the flow consists of the compressible Euler equations. The solver reduces the flowfield inside multistage axial compressors or turbines to its description on the meridional plane (Fig. 3). This reduction is obtained by assuming that the flowfield is axisymmetric and the blades have vanishing thickness and infinite solidity, so that each single blade coincides with a stream surface. The flow deflection through the stators and rotors is the result of the forces that the blades exert on the flow: This effect is modeled by volume forces orthogonal to the stream surfaces. These are typical hypotheses of through-flow codes and are reasonably verified in usual turbomachine configurations, where the number of blades is such that the solidity is high. In our approach, instead of modifying the blade shape, as a classical shape optimization does, we give the force that the blades exert to the flow, and let the geometry accommodate this distribution of forces by solving an inverse problem. The volume force distribution is then updated according to an adjoint optimization process, so that the objective functional, for example, the thrust, is maximized.[9] Although a simpler, but less complete, flow model could enhance the readability of the paper, the authors prefer to explain the background that has inspired the BC model and the practical design problems that they aim to overcome.

In a cylindric frame of reference, the compressible Euler equations with volume forces acting on the fluid are

$$\frac{\partial \boldsymbol{U}}{\partial t} + \frac{\partial \boldsymbol{A}}{\partial x} + \frac{\partial \boldsymbol{B}}{\partial r} + \boldsymbol{Q} = 0, \qquad (x, r) \in \Omega \tag{21}$$

where $\boldsymbol{U} = \{\rho, \rho u, \rho v, \rho w, e\}^T$ and

$$\boldsymbol{A} = \begin{Bmatrix} \rho u \\ p + \rho u^2 \\ \rho u v \\ \rho u w \\ u(p+e) \end{Bmatrix}, \qquad \boldsymbol{B} = \begin{Bmatrix} \rho w \\ \rho u w \\ \rho v w \\ p + \rho w^2 \\ w(p+e) \end{Bmatrix}$$

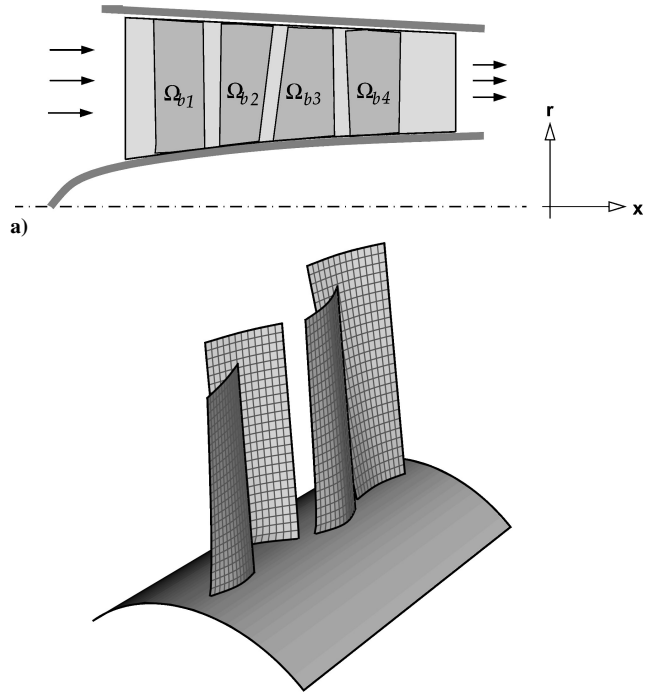

Fig. 3 Schematic of multistage turbomachine a) meridional plane (areas Ω_b are projections of blade surfaces onto the meridional plane) and b) a three-dimensional view of the blade surfaces.

$$\boldsymbol{Q} = \begin{Bmatrix} \rho w/r \\ \rho u w/r - F^x \\ 2\rho v w/r - F^\theta \\ \rho(w^2 - v^2)/r - F^r \\ w(p+e)/r - \boldsymbol{F}\cdot\boldsymbol{q} \end{Bmatrix}$$

System (21) is approximated using a finite volume technique by discretizing the computational domain with four-sided cells. The integration in time is carried out according to a Godunov-type two-step scheme. A standard first-order flux difference splitting is used at the predictor step: The conservative variables $\boldsymbol{U}$ are assumed as an averaged, constant value inside each cell. The fluxes $\boldsymbol{A}$ and $\boldsymbol{B}$ are evaluated by solving the Riemann problems that are pertinent to the discontinuities that occur at the cell interfaces. The approximate Riemann solver suggested by Pandolfi[11] was adopted for this purpose. At the corrector level, second-order accuracy is achieved by assuming a linear, instead of constant, behavior of the primitive variables inside the cells, according to the essentially nonoscillatory schemes.[16] The resulting scheme is second-order accurate in both time and space.

Adjoint Optimization

Here we deal with the general case of an optimization procedure that enforces the RIB BCs, through penalization, and also seeks the maximum of a certain performance. To enforce only the BCs, the term expressing the performance must be removed. As already mentioned, the starting point of our implementation of the RIB set of BCs is an existing tool for shape optimization that combines an inverse problem solver with an adjoint optimization procedure. See Refs. 9, 13, and 14 for more details on the coupling between inverse problems and adjoint optimization. For a general approach to shape optimization, see Refs. 17–20.

Let us now suppose that we are looking for aerodynamic solutions that maximize the thrust. If conventional BCs are used, the objective functional would be

$$\mathcal{H} = \int_{\Gamma_o} (p + \rho u^2)\,\mathrm{d}\Gamma - \int_{\Gamma_i} (p + \rho u^2)\,\mathrm{d}\Gamma \tag{22}$$

where $\mathcal{H}$ represents the conventional thrust. When using the RIB BCs, the objective functional is penalized as

$$\mathcal{T} = \mathcal{H} - \frac{\chi_1}{2}\mathcal{B}_i - \frac{\chi_2}{2}\mathcal{B}_o$$
$$= \mathcal{H} - \frac{\chi_1}{2}\int_{\Gamma_i}(T^0 - \bar{T}^0)^2\,\mathrm{d}\Gamma - \frac{\chi_2}{2}\int_{\Gamma_o}(M_x - \overline{M_x})^2\,\mathrm{d}\Gamma \quad (23)$$

where $\bar{T}^0$ and $\overline{M_x}$ are the target total temperature at the inlet and the axial Mach number at the outlet. Although a constant level of the total temperature seems to be the most adequate BC at the inlet, several choices at the outlet are possible. For instance, we implemented the following alternative functionals:

$$\mathcal{B}_o^I = \int_{\Gamma_o}(p - \overline{p})^2\,\mathrm{d}\Gamma \quad (24)$$

$$\mathcal{B}_o^{II} = \int_{\Gamma_o}(\rho u - \overline{\rho u})^2\,\mathrm{d}\Gamma \quad (25)$$

$$\mathcal{B}_o^{III} = \left[\int_{\Gamma_o}\rho u\,\mathrm{d}\Gamma - \int_{\Gamma_o}\overline{\rho u}\,\mathrm{d}\Gamma\right]^2 \quad (26)$$

The term $\mathcal{B}_o^I$ corresponds to imposing the static pressure at the outlet. Terms $\mathcal{B}_o^{II}$ and $\mathcal{B}_o^{III}$ impose a local or global constraint on the mass flow at the outlet, respectively.

The distributed control is represented by the tangential forces F^θ and by the Riemann invariants R_{1o} on the cell interfaces at the outlet boundary and R_{3i} at the inlet. The tangential forces F^θ are null everywhere except on the blades, where they are only discretized along the radial direction as

$$F^\theta(x, r_i) = \mathcal{F}(r_i)(1 - \cos\{2\pi[(x - x_t)/(x_l - x_t)]\}) \quad (27)$$

so that the load on the leading ($x = x_l$) and trailing ($x = x_t$) edges is 0. For each blade row, there are as many design parameters $\mathcal{F}(r_i)$ as the number of computational points in the radial direction. The maximum of $\mathcal{T}$ is constrained by the steady-state Euler equations:

$$\boldsymbol{E}(F^\vartheta) = \boldsymbol{A}_x + \boldsymbol{B}_r + \boldsymbol{Q} = 0 \quad (28)$$

Another constraint is related to the blade equation of motion.[9] The blade surface, defined as $\vartheta = g(x, r, t)$, is one of the unknowns of the problem, and its shape changes in time according to a kinematic relation that ensures the impermeability of such a surface, that is,

$$g_t = ug_x + wg_r - (v - \omega r)/r \quad (29)$$

This relation links the time derivative g_t and spatial derivatives g_x and g_r to the flow variables and to the rotational speed ω. It also represents an additional constraint for the optimization problem,

$$G[\boldsymbol{U}(F^\vartheta)] = ug_x + wg_r - (v - \omega r)/r = 0 \quad (30)$$

To solve this constrained maximization problem, we introduce the Lagrangian function

$$\mathcal{L}(\boldsymbol{U}, g, F^\vartheta, \Lambda, \mu, \xi_i, \xi_o) = \mathcal{T} + \int_\Omega {}^t\boldsymbol{\Lambda}\boldsymbol{E}(\boldsymbol{U}, F^\vartheta, g)\,\mathrm{d}\Omega$$
$$+ \int_\Omega \mu G(\boldsymbol{U}, g)\,\mathrm{d}\Omega + \int_{\Gamma_i}\xi_i(R_{3i} - \overline{R_{3i}})\,\mathrm{d}\Gamma$$
$$+ \int_{\Gamma_o}\xi_o(R_{1o} - \overline{R_{1o}})\,\mathrm{d}\Gamma \quad (31)$$

where ${}^t\Lambda(x, r) = (\lambda_1, \lambda_2, \lambda_3, \lambda_4, \lambda_5)$, $\mu = \mu(x, r)$, $\xi_i = \xi_i(x, r)$, and $\xi_o = \xi_o(x, r)$ are Lagrange multipliers. The Lagrangian will allow the maximization problem to be treated as an unconstrained problem. A stationary point is found when the variations of $\mathcal{L}$ vanish with respect to all of its arguments. We have

$$\delta\mathcal{L} = \delta\mathcal{L}_U + \delta\mathcal{L}_{F^\vartheta} + \delta\mathcal{L}_g + \delta\mathcal{L}_\Lambda + \delta\mathcal{L}_\mu + \delta\mathcal{L}_{\xi_i}$$
$$+ \delta\mathcal{L}_{\overline{R_{3i}}} + \delta\mathcal{L}_{\xi_o} + \delta\mathcal{L}_{\overline{R_{1o}}} \quad (32)$$

where

$$\delta\mathcal{L}_U = \frac{\partial\mathcal{T}}{\partial\boldsymbol{U}}\delta\boldsymbol{U} + \int_\Omega {}^t\boldsymbol{\Lambda}\delta\boldsymbol{E}_U\,\mathrm{d}\Omega + \int_\Omega \mu\frac{\partial G}{\partial\boldsymbol{U}}\delta\boldsymbol{U}\,\mathrm{d}\Omega \quad (33)$$

$$\delta\mathcal{L}_g = \int_\Omega {}^t\boldsymbol{\Lambda}\delta\boldsymbol{Q}_g\,\mathrm{d}\Omega + \int_\Omega \mu\delta G_g\,\mathrm{d}\Omega \quad (34)$$

$$\delta\mathcal{L}_\Lambda = \int_\Omega {}^t\delta\boldsymbol{\Lambda}\boldsymbol{E}(\boldsymbol{U}, F^\vartheta, g)\,\mathrm{d}\Omega \quad (35)$$

$$\delta\mathcal{L}_\mu = \int_\Omega G(\boldsymbol{U}, g)\delta\boldsymbol{\mu}\,\mathrm{d}\Omega \quad (36)$$

$$\delta\mathcal{L}_{F^\vartheta} = \int_\Omega {}^t\boldsymbol{\Lambda}\frac{\partial\boldsymbol{Q}}{\partial F^\vartheta}\delta F^\vartheta\,\mathrm{d}\Omega \quad (37)$$

$$\delta\mathcal{L}_{\overline{R_{1o}}} = -\int_{\Gamma_o}\xi_o\delta\overline{R_{1o}}\,\mathrm{d}\Gamma \quad (38)$$

$$\delta\mathcal{L}_{\overline{R_{3i}}} = -\int_{\Gamma_i}\xi_i\delta\overline{R_{3i}}\,\mathrm{d}\Gamma \quad (39)$$

$$\delta\mathcal{L}_{\xi_i} = \int_{\Gamma_i}\delta\xi_i(R_{3i} - \overline{R_{3i}})\,\mathrm{d}\Gamma \quad (40)$$

$$\delta\mathcal{L}_{\xi_o} = \int_{\Gamma_o}\delta\xi_o(R_{1o} - \overline{R_{1o}})\,\mathrm{d}\Gamma \quad (41)$$

To have $\delta\mathcal{L} = 0$, all of the single contributions to $\delta\mathcal{L}$ must vanish at the maximum, so that we enforce

$$\delta\mathcal{L}_U = 0, \qquad \delta\mathcal{L}_g = 0, \qquad \delta\mathcal{L}_\Lambda = 0$$
$$\delta\mathcal{L}_\mu = 0, \qquad \delta\mathcal{L}_{\xi_i} = 0, \qquad \delta\mathcal{L}_{\xi_o} = 0 \quad (42)$$

In general, this results in

$$\delta\mathcal{L}_{F^\vartheta} \neq 0, \qquad \delta\mathcal{L}_{\overline{R_{3i}}} \neq 0, \qquad \delta\mathcal{L}_{\overline{R_{1o}}} \neq 0 \quad (43)$$

To reach the maximum δF^ϑ, $\delta\overline{R_{3i}}$ and $\delta\overline{R_{1o}}$ are taken so that

$$\delta\mathcal{L}_{F^\vartheta} > 0, \qquad \delta\mathcal{L}_{\overline{R_{3i}}} > 0, \qquad \delta\mathcal{L}_{\overline{R_{1o}}} > 0 \quad (44)$$

for example, using a conjugate gradient method.[17]

Note that the variations of $\mathcal{L}$ with respect to the Lagrange multipliers Λ, ξ_i, ξ_o, and μ simply yield the flow equations and the constraint enforcement. For the term $\delta\mathcal{L}_U$, we can manipulate the second integral in Eq. (31) and obtain

$$\delta\mathcal{L}_U = \frac{\partial\mathcal{T}}{\partial\boldsymbol{U}}\delta\boldsymbol{U} + \int_\Gamma {}^t\boldsymbol{\Lambda}(\boldsymbol{A}_U n_x + \boldsymbol{B}_U n_r)\delta\boldsymbol{U}\,\mathrm{d}\Gamma$$
$$- \int_\Omega ({}^t\boldsymbol{\Lambda}_x\boldsymbol{A}_U + {}^t\boldsymbol{\Lambda}_r\boldsymbol{B}_U)\delta\boldsymbol{U}\,\mathrm{d}\Omega + \int_\Omega {}^t\boldsymbol{\Lambda}\frac{\partial\boldsymbol{Q}}{\partial\boldsymbol{U}}\delta\boldsymbol{U}\,\mathrm{d}\Omega$$
$$+ \int_\Omega \mu\frac{\partial G}{\partial\boldsymbol{U}}\delta\boldsymbol{U}\,\mathrm{d}\Omega \quad (45)$$

where Γ is the entire border of the flowfield Ω, and $\boldsymbol{A}_U$, $\boldsymbol{B}_U$, and $\boldsymbol{Q}_U$ are Jacobian matrices. From $\delta\mathcal{L}_U = 0$, we obtain the so-called adjoint of the Euler equations, that is,

$${}^t\boldsymbol{\Lambda}_x\boldsymbol{A}_U + {}^t\boldsymbol{\Lambda}_r\boldsymbol{B}_U - {}^t\boldsymbol{\Lambda}\frac{\partial\boldsymbol{Q}}{\partial\boldsymbol{U}} - \mu\frac{\partial G}{\partial\boldsymbol{U}} = 0 \quad (46)$$

on the domain Ω, and also the related conditions

$$\left[\frac{\partial \mathcal{I}}{\partial \boldsymbol{U}} + {}^t\boldsymbol{\Lambda}(\boldsymbol{A}_U n_x + \boldsymbol{B}_U n_r) + \xi_i \frac{\partial R_{3i}}{\partial \boldsymbol{U}} + \xi_o \frac{\partial R_{1i}}{\partial \boldsymbol{U}}\right]\delta \boldsymbol{U} = 0 \quad (47)$$

on its boundary Γ with unit normal vector $\boldsymbol{n} = (n_x, n_r)$.

The condition $\delta \mathcal{L}_g = 0$ yields

$$\delta \mathcal{L}_g = \int_{\Omega_b} \mu \delta G_g \,\mathrm{d}\Omega + \int_{\Omega_b} {}^t\boldsymbol{\Lambda}\delta \boldsymbol{Q}_g \,\mathrm{d}\Omega = \int_{\Gamma_b} \mu(\boldsymbol{q}\cdot\boldsymbol{n})\delta g \,\mathrm{d}\Gamma$$
$$- \int_{\Omega_b} [(\mu u)_x + (\mu u)_r]\delta g \,\mathrm{d}\Omega + \int_{\Omega_b} {}^t\boldsymbol{\Lambda}\delta \boldsymbol{Q}_g \,\mathrm{d}\Omega = 0 \quad (48)$$

Hence, the adjoint of the kinematic constraint in Ω_b is

$$(\mu u)_x + (\mu u)_r + \nabla \cdot ({}^t\boldsymbol{\Lambda}\boldsymbol{K}) = 0 \quad (49)$$

together with the BC on Γ_b

$$[\mu(\boldsymbol{q}\cdot\boldsymbol{n}) + ({}^t\boldsymbol{\Lambda}\boldsymbol{K})\cdot\boldsymbol{n}]\delta g = 0 \quad (50)$$

where

$$\boldsymbol{K} = rF^{\vartheta}\begin{bmatrix} 0 & 0 \\ 1 & 0 \\ 0 & 0 \\ 0 & 1 \\ u & w \end{bmatrix} \quad (51)$$

The adjoint equation of the kinematic constraint is coupled to Eq. (46) the same way the kinematic constraint is coupled to the flow equations.

Flow Adjoint BC

The method that is used to derive the BCs for the flow adjoint equation and the kinematic constraint adjoint equation is explained in detail.

At the inlet, Eq. (47) reduces to

$$\left[\frac{\partial \mathcal{T}}{\partial \boldsymbol{U}} + {}^t\boldsymbol{\Lambda}\boldsymbol{C}_U + \xi_i \frac{\partial R_3}{\partial \boldsymbol{U}}\right]\delta \boldsymbol{U} = 0 \quad (52)$$

with $\boldsymbol{C} = \boldsymbol{A}_U n_x + \boldsymbol{B}_U n_r$. Because the flow variables $\boldsymbol{U}$ have to respect given conditions at the boundaries, the variation $\delta\boldsymbol{U}$ at the inlet is such that the BCs on $\boldsymbol{U}$ are still satisfied. For example, if the inlet flow is supersonic all of the components of $\boldsymbol{U}$ are given. In this case $\delta\boldsymbol{U} = 0$, and consequently, there is no BC on $\boldsymbol{\Lambda}$.

In the case of subsonic inlet, four BCs should be provided. Each BC incorporated in the objective function must be subtracted from this count. For example, we included the total temperature at the inlet in the optimization process, so that only three conditions have to be provided. Let us impose

$$\mathrm{d}S = 0, \qquad \mathrm{d}\sigma = 0, \qquad \mathrm{d}\epsilon = 0 \quad (53)$$

where

$$S = \log(p/\rho) - 2\kappa \log \rho, \qquad \sigma = v/u, \qquad \epsilon = w/u \quad (54)$$

and where we set $\boldsymbol{U} = (\rho, \rho u, \rho v, \rho w, e) = (u_1, u_2, u_3, u_4, u_5)$. We obtain

$$\delta S = \frac{\partial S}{\partial u_1}\delta u_1 + \frac{\partial S}{\partial u_2}\delta u_2 + \frac{\partial S}{\partial u_3}\delta u_3 + \frac{\partial S}{\partial u_4}\delta u_4 + \frac{\partial S}{\partial u_5}\delta u_5 = 0$$
$$\delta\sigma = \frac{\partial \sigma}{\partial u_2}\delta u_2 + \frac{\partial \sigma}{\partial u_3}\delta u_3 = 0, \qquad \delta\epsilon = \frac{\partial \epsilon}{\partial u_2}\delta u_2 + \frac{\partial \epsilon}{\partial u_4}\delta u_4 = 0 \quad (55)$$

From the decomposition $\boldsymbol{C} = \boldsymbol{RDL}$, where $\boldsymbol{D}$ is a diagonal matrix that contains the eigenvalues of $\boldsymbol{C}$ and $\boldsymbol{R}$ and $\boldsymbol{L}$ are the matrices of the corresponding right and left eigenvectors, we also obtain $\delta\boldsymbol{W} = \boldsymbol{L}\delta\boldsymbol{U}$ and $\delta\boldsymbol{U} = \boldsymbol{R}\delta\boldsymbol{W}$. Equation (52) can be rewritten as

$$\left[\frac{\partial \mathcal{T}}{\partial \boldsymbol{U}}\boldsymbol{R} + {}^t\boldsymbol{\Lambda}\,\boldsymbol{RD} + \xi_i \frac{\partial R_3}{\partial \boldsymbol{U}}\boldsymbol{R}\right]\delta\boldsymbol{W} = 0 \quad (56)$$

where the generic increment $\delta\boldsymbol{W}$ can be expressed by δR_1 and δR_3:

$$\delta\boldsymbol{W} = \boldsymbol{J}_{\mathrm{in}}\begin{Bmatrix} \delta R_1 \\ \delta R_3 \end{Bmatrix}, \qquad \boldsymbol{J}_{\mathrm{in}} = \begin{bmatrix} 0 & 0 \\ -\sigma/2 & \sigma/2 \\ -\epsilon/2 & \epsilon/2 \\ 1 & 0 \\ 0 & 1 \end{bmatrix} \quad (57)$$

so that

$$\left[\frac{\partial \mathcal{T}}{\partial \boldsymbol{U}}\boldsymbol{R} + {}^t\boldsymbol{\Lambda}\,\boldsymbol{RD} + \xi_i \frac{\partial R_3}{\partial \boldsymbol{U}}\boldsymbol{R}\right]\boldsymbol{J}_{\mathrm{in}}\begin{Bmatrix} \delta R_1 \\ \delta R_3 \end{Bmatrix} = 0 \quad (58)$$

These are two scalar relations that have to be satisfied by the component of $\boldsymbol{\Lambda}$ and by ξ_i.

The situation is reversed at the outlet. For a supersonic outlet, we pose $\boldsymbol{\Lambda} = 0$, whereas for a subsonic outlet we obtain

$$\left[\frac{\partial \mathcal{T}}{\partial \boldsymbol{U}} + {}^t\boldsymbol{\Lambda}\boldsymbol{C} + \xi_o \frac{\partial R_1}{\partial \boldsymbol{U}}\right]\delta\boldsymbol{U} = 0 \quad (59)$$

which is a set of five relations for $\boldsymbol{\Lambda}$ and ξ_o at the outlet boundary.

For the sake of completeness, we recall that, according to Ref. 9, the BCs on the top and bottom walls are simply

$$n_x\lambda_2 + n_r\lambda_4 = 0 \quad (60)$$

For the kinematic adjoint at the blade leading edge, $\delta g = 0$; therefore Eq. (50) is satisfied. At the trailing edge, there is no constraint on

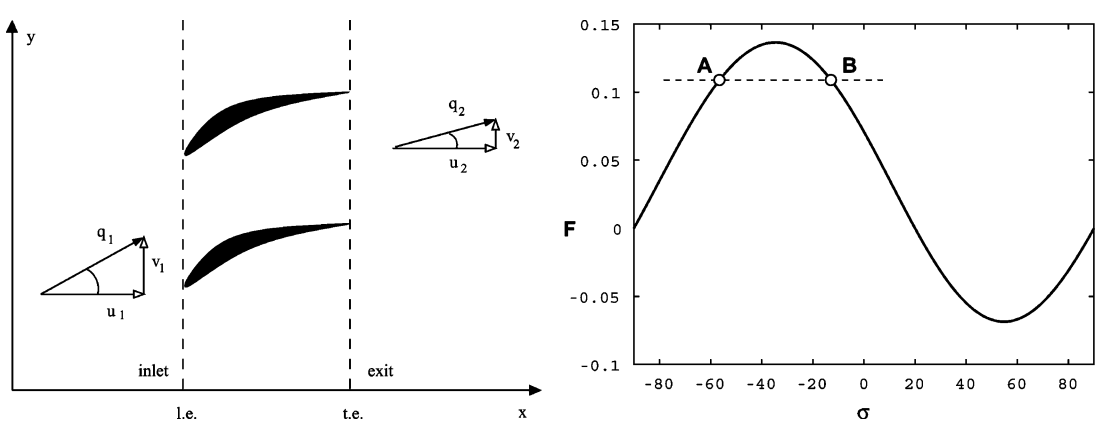

Fig. 4 One-dimensional model of a stator cascade: a) model and b) typical diagram of the blade force vs flow deflection σ.

δg, hence, on Γ_b

$$[\mu(\boldsymbol{q}\cdot\boldsymbol{n}) + ({}^t\boldsymbol{\Lambda}\boldsymbol{K})\cdot\boldsymbol{n}] = 0 \tag{61}$$

which is the BC for the adjoint equation.

Numerical Results

The performances of the numerical algorithm are investigated. The main goal is to highlight the advantages and drawbacks of the design procedure that enforces the new BCs with respect to the original formulation, explained in Ref. 9, in which conventional BCs were used.

Single Stator Design

One mechanism which leads an inverse problem to fail is related to the non-uniqueness of the solution within certain BCs. This problem has been focused on in NACA CR 3836[7] with the aid of a theoretical example. Let us consider a one-dimensional axisymmetric model of

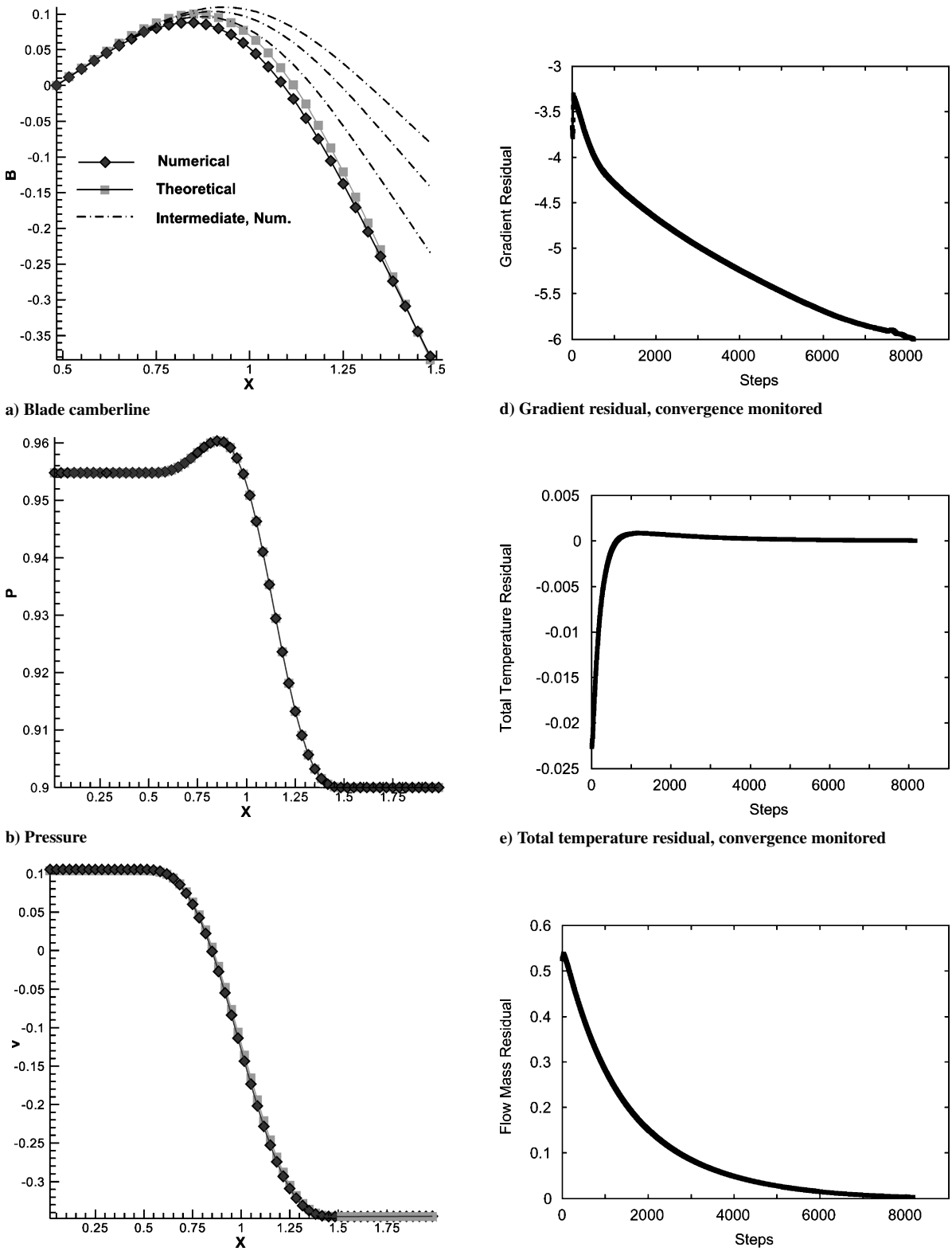

a) Blade camberline

b) Pressure

c) Tangential velocity

d) Gradient residual, convergence monitored

e) Total temperature residual, convergence monitored

f) Exit mass flow residual, convergence monitored

Fig. 5 Single stator design; configuration A, unstable to conventional BCs: △, numerical and □, theoretical.

a stator blade in a duct, as shown in Fig. 4. The total temperature, total pressure, and flow angle are imposed at the inlet, whereas the exit static pressure is given at the outlet. The theoretical solution of the one-dimensional problem is shown in Fig. 4. It can be seen that a solution exists only for a given range of blade forces. Moreover, in this range, two solutions exists for a given blade force, labeled A and B in Fig. 4b. Solution A with the higher deflection is inherently unstable, as discussed in detail in Ref. 7. When the inverse problem is numerically solved with the earlier mentioned BCs, it converges naturally to configuration B. It is also shown in Ref. 7 that the two solutions are characterized by different mass flows and that one way of solving this problem is to fix the exit mass flow, instead of the static pressure, so that the blade force becomes a single value, monotonic function of the exit conditions. The inverse problem pertinent to the two configurations has been solved numerically by Zannetti and Pandolfi[7] for the one-dimensional case, using an unconventional

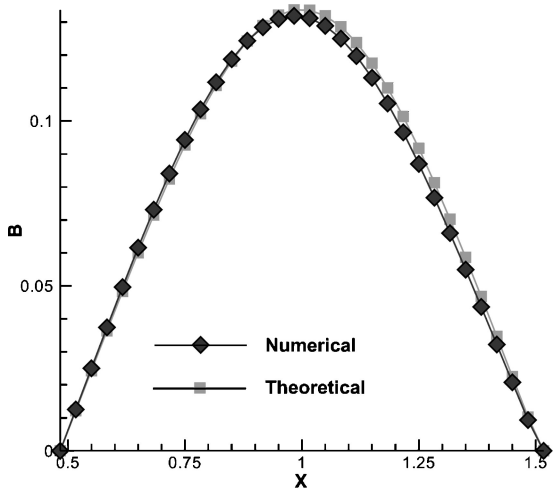

a) Blade camberline

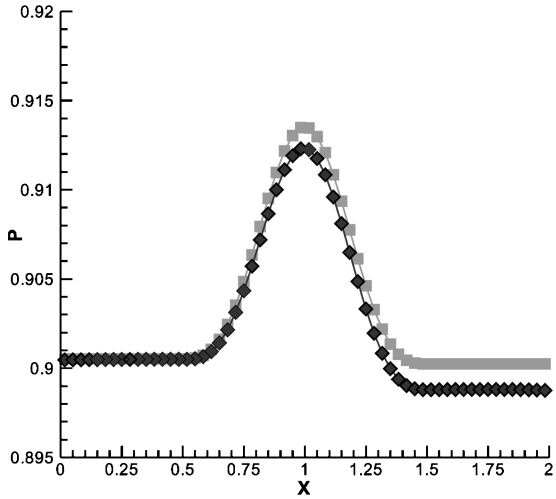

b) Pressure

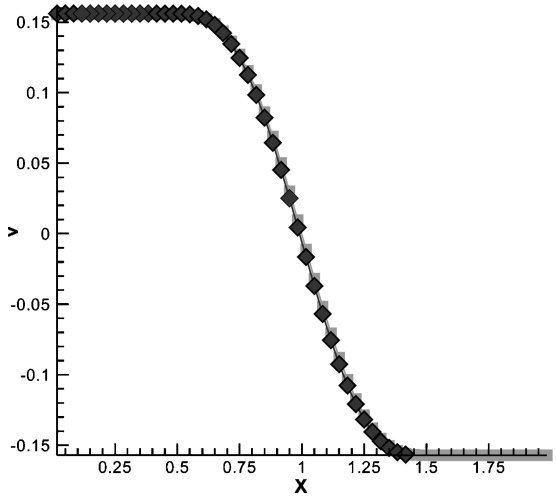

c) Tangential velocity

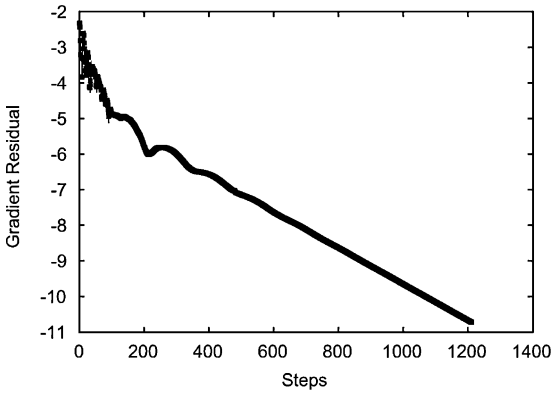

d) Gradient residual, convergence monitored

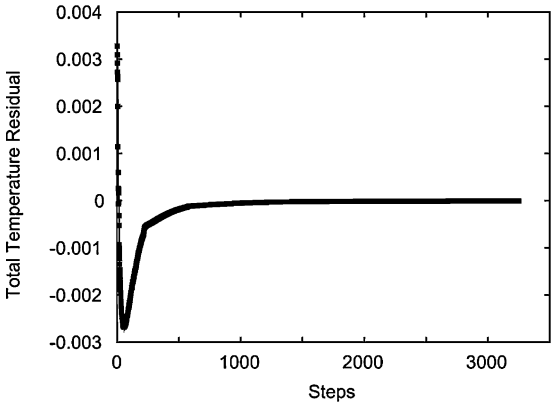

e) Total temperature residual, convergence monitored

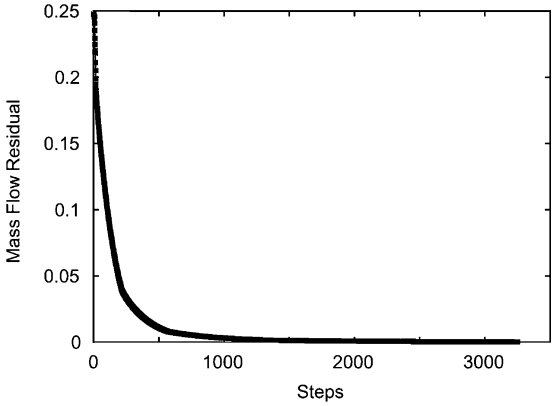

f) Exit mass flow residual, convergence monitored

Fig. 6 Single stator design, configuration B, stable to conventional BCs: △, numerical and □ theoretical.

BC, which fixes the exit mass flow. Unfortunately, the extension of this BC to two-dimensional inverse problems for cascades has resulted in serious convergence problems.

The RIB numerical procedure here proposed is able to overcome these stability problems, and the two solutions are correctly obtained. The results that are pertinent to the solution of the NASA CR 3836 test are shown in Fig. 5 for configuration A and in Fig. 6 for configuration B. The total temperature at the inlet and the mass flow at the outlet have been enforced using the RIB procedure, whereas the other BC has been implemented in a standard way. The enforcement of the RIB BCs is reached through an iterative process. This process was stopped when the gradient residual was decreased by three orders of magnitude and the error on the target BC was less than 0.1%. The blade geometry and the pressure and velocity distributions are compared with their theoretical values in Figs. 5a–5c and Figs. 6a–6c. Convergence to the theoretical solution is reached monotonically, as can be seen from the convergence history of the gradient residuals.

Algorithm Performances

A comparison with conventional BCs has been performed to analyze the performances of the RIB BCs in solving the inverse problem. Configuration B of NACA CR3836 has been adopted as a reference test case because it is stable with the conventional condition on the exit static pressure. In our computations, the test case has been made two dimensional by giving a radial extension to the stator blade ($1 \leq r/c \leq 1.5$), where c is the axial chord length. In the computations using the conventional BC, the total temperature at the inlet and the exit static pressure were imposed, whereas for the RIB procedure the value of the Riemann invariants at the inlet and outlet were chosen so that, at the steady state, the same levels of total temperature and pressure of the preceding case were also matched at the boundary. The performances are summarized in Table 1 for different grid sizes. Because each time step requires the same CPU time for both of the procedures, the performances are expressed by the number of time steps required to reach the convergence of the inverse problem. The steady state is here conventionally reached when the L^2 norm of the flow variable residual is less than 10^{-7}. The nondimensional time is also monitored in the simulations, to check the duration of the transient.

From Table 1, we can observe that, with the new BCs, the transient is greatly reduced in time, being about five times shorter. As a consequence, the number of time steps to convergence, that is, the CPU time, is reduced accordingly. The main drawback of the RIB procedure is that the correct value of the Riemann invariant that matches the target BC is unknown, and in general this match can be obtained only through an iterative process, by solving a minimization problem. The new BCs speed up the calculations of the inverse problem, but they satisfy the target BCs asymptotically, through an iterative updating of the Riemann invariants at the border. This process, as currently implemented by the authors, is driven by a line-seek algorithm based on a Polak–Ribiere nonlinear conjugate gradient method. The functional gradient is evaluated via the flow equation adjoint.[9] From numerical experiments, it can be observed that the global procedure does not converge as fast as the inverse problem solution using a standard BC treatment. This lack of performances is, however, compensated for by a higher reliability of the solver when using the RIB BCs.

Table 1 Inverse problem convergence: comparison of the performances between the two sets of BCs

	Conventional BC		New BC	
Grid size	Steps	Time	Steps	Time
20 × 5	5,190	65.466	1,388	16.213
40 × 10	10,432	65.397	2,566	14.967
80 × 20	25,558	79.811	4,860	13.987
160 × 40	49,860	78.977	9,010	13.120

Fan Stage Design

The use of the overall procedure becomes computationally more advantageous when the aerodynamic design does not reduce to a pure inverse problem, but an optimization process is also involved. Nevertheless, it must be stressed that the comparison of the performance of the two earlier mentioned approaches to boundary treatment remains essentially problem dependent. Because the RIB BC enforcement already involves an optimization, an ulterior maximization/minimization of target performance is paid at the cost of a penalization procedure, so that any gap with an analogous shape optimization approach that uses conventional boundary treatment should be greatly reduced. The aerodynamic design of a fan stage was selected as a reference task for the comparison. The design parameters were chosen so that the inverse problem, using conventional BCs,

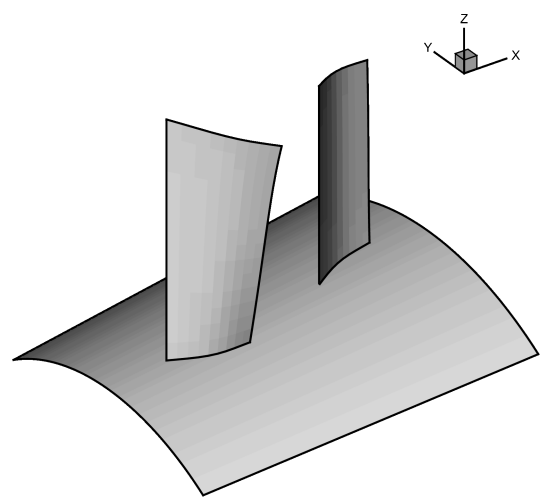

Fig. 8 Fan blade optimization; final blade geometry.

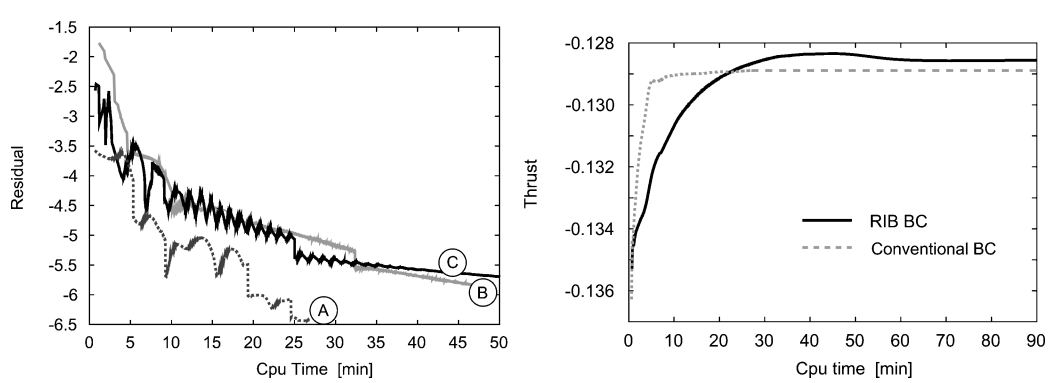

a) b)

Fig. 7 Fan blade optimization: a) gradient residual comparison for A optimization with conventional BCs, B inverse problem solution with RIB BCs, and C optimization with RIB BCs and b) thrust optimization history for cases A and C.

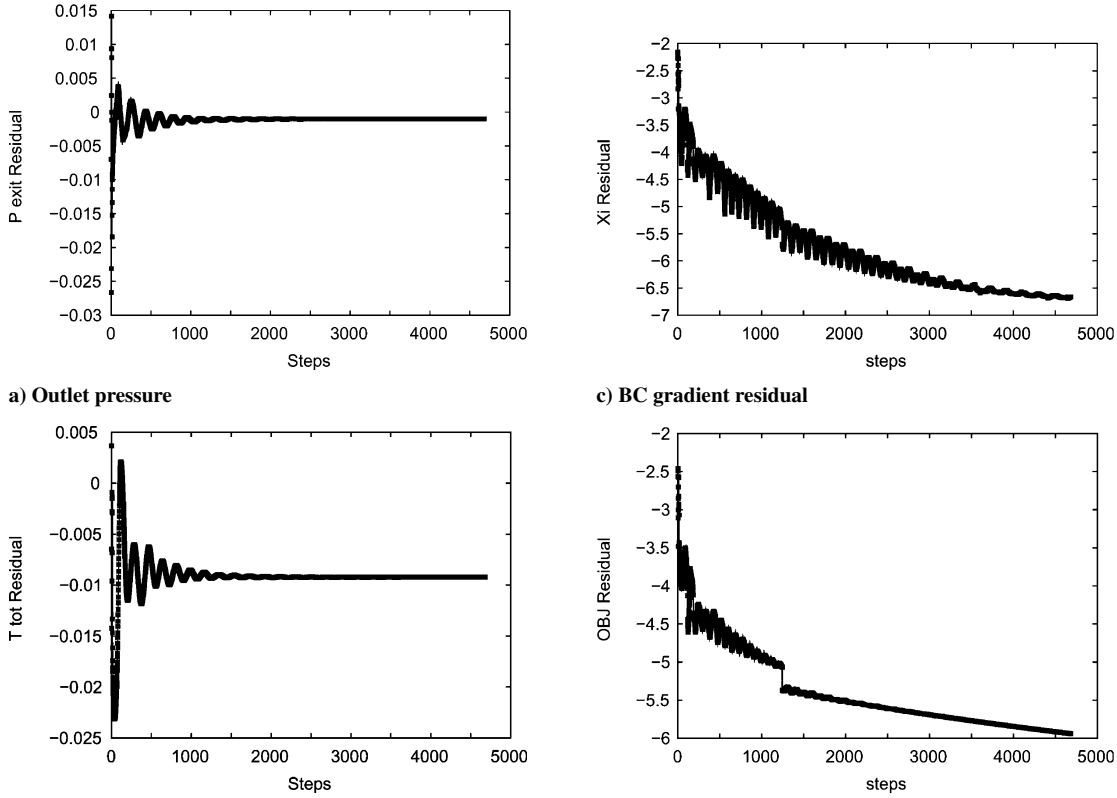

a) Outlet pressure

c) BC gradient residual

b) Inlet total temperature

d) Objective functional residual

Fig. 9 Fan blade optimization; history of various residuals to monitor convergence.

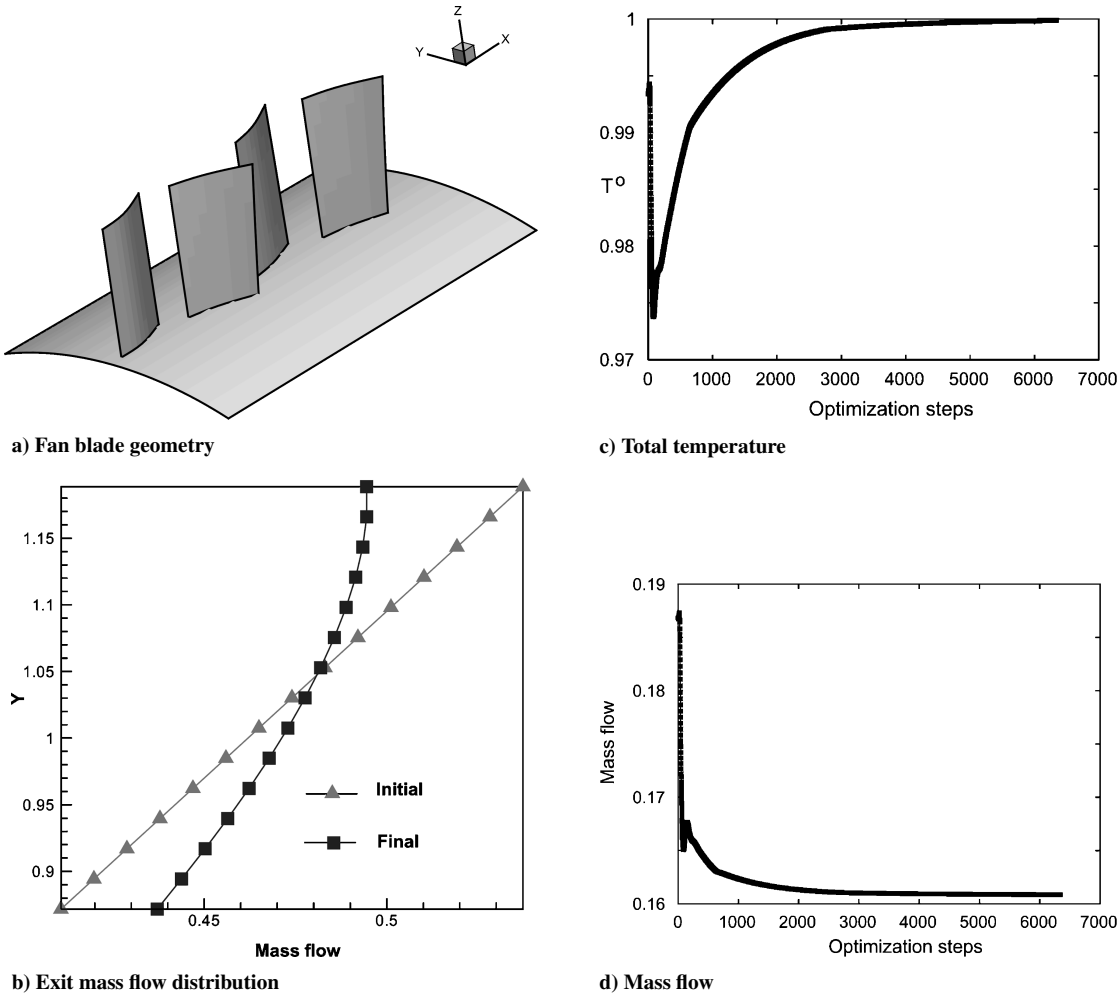

a) Fan blade geometry

c) Total temperature

b) Exit mass flow distribution

d) Mass flow

Fig. 10 Inverse problem over two-stage turbine; global mass flow prescribed at the outlet as the exit BC.

converges. Three cases are presented: 1) fan blade optimization for thrust using conventional BCs (case A), 2) inverse problem solution using RIB boundary conditions (case B), and fan blade optimization for thrust using RIB boundary conditions (case C)

The test does not take into account the different number of control parameters for the three cases. If we consider that the radial grid spacing adopted is $mc = 25$ and that the fan stage has $n_{\mathrm{br}} = 2$ blade rows, the number of parameters one has to optimize is $n_{\mathrm{br}} \times mc = 50$ for case A, $2 \times mc = 50$ for case B, and $n_{\mathrm{br}} \times (mc + 2) = 54$ for case C. The convergence history of the gradient residual vs the CPU time is given in Fig. 7. The timing has been performed on an Athlon XP2000-based personal computer. Again, as can be seen, the case with conventional BCs converges more rapidly, whereas the inverse problem solution and the optimization using thee Riemann-based BCs show comparable CPU time requirements. Because the gradient residual for cases B and C is relatively smooth, it could be argued that an adaptive stepping procedure for the conjugate gradient method could enhance the convergence rate. Figure 7 also shows the time history of the thrust during the optimization cycles for cases A and C, whereas the thrust of case B coincides with the first point of the curve for the conventional BCs. The asymptotic value of the thrust should be the same for the two cases. In the numerical simulations this value shows a slight dependence on the relative weights χ_i and χ_o that were adopted for the penalization of the objective function so that a higher thrust could temporarily result from a weaker enforcement of the BC. The optimization process with the RIB BC was stopped when the residual of the thrust and of the BCs decreased at least by three orders of magnitude.

The final blade geometry and the converge history of all of these variables are shown in Figs. 8 and 9. As a final consideration, note that all of the computations here presented have required CPU times that ranged from several minutes to some hours on an entry level workstations or a desktop personal computer, as in the case of multistage axial machine optimization.

Inverse Problem on a Two-Stage Turbine

Another remarkable feature of the new procedure is that not only local BCs can be imposed but also integral formulations along the boundary. For example, instead of prescribing the value of the mass flow rate on the boundary point by point, by the adoption of a functional such as $\mathcal{B}_o^{II}$ of Eq. (25), the global mass flow can be set at the outlet by using a functional as $\mathcal{B}_o^{III}$ of Eq. (26). The mentioned BC results in a weaker constraint rather than when the local mass flow is fixed at each boundary point because the system has a degree of freedom more in the optimization space. The optimization process will automatically select the optimal mass flow distribution. This feature has not any equivalent in conventional BCs. As an example, Fig. 10 refers to the design of a two-stage turbine via the inverse problem solution. The Riemann-based BCs on the total temperature has been adopted at the inlet, whereas global mass was prescribed at the outlet. The initial and final mass flow distributions are shown in Fig. 10b.

Conclusions

Motivated by well-posedness requirements of inverse design methodologies, we focused our attention on the effects of boundary reflectiveness. The mechanism of reflection of an incident perturbation has been investigated through an analysis of the characteristic wave system in proximity of the flowfield boundary. Adopting a nonlinear, isentropic model for the wave propagation system, a parameter was defined as the ratio of the incident and reflected signal strengths, to measure the reflectiveness of various BCs. A method of breaking up the reflection mechanism, based on the direct modelization of the boundary response, was then proposed. The new set of nonreflecting BCs was investigated and integrated in a design procedure that combines an inverse problem solution and adjoint optimization. Numerical experiments have shown that such conditions are quite effective in solving the inverse problem, although the related penalization delays convergence of the adjoint procedure due to the increased number of optimization parameters. Nevertheless, the convergence of the whole numerical procedure is affected by both phenomena and the advantages over conventional BCs should be evaluated case by case. When a conventional BC can be used, the numerical experiments suggest that inverse problems using conventional BCs are solved faster than when using the RIB set. Conversely, RIB BCs enhance the robustness of the code and require a computational effort that is sustainable even for low-entry workstations. The two sets of BCs are, however, not equivalent in the sense that the RIB set of BCs has proved to be effective where the conventional one can be deleterious. The RIB set also allows combinations of fluid dynamic variables or integral formulations to be imposed along the whole boundary, combinations that have no equivalent conventional BC.

References

[1]Kreiss, H., "Initial Boundary Value Problem for Hyperbolic Systems," *Communications in Pure and Applied Mathematics*, Vol. 23, 1970, pp. 277–298.

[2]Engquist, B., and Majda, A., "Absorbing Boundary Conditions for the Numerical Simulation of Waves," *Mathematics of Computation*, Vol. 31, 1977, pp. 629–651.

[3]Thompson, P., "Time Dependent Boundary Conditions for Hyperbolic Systems, *Journal of Computational Physics*, Vol. 68, 1987, pp. 1–24.

[4]Giles, M., "Nonreflecting Boundary Conditions for Euler Equations Calculations, *AIAA Journal*, Vol. 28, 1990, pp. 2050–2058.

[5]Poinsot, T., and Lele, S., "Boundary Conditions for Direct Simulations of Compressible Viscous Reacting Flows," *Journal of Computational Physics*, Vol. 101, 1992, pp. 104–129.

[6]Lighthill, J. M., "A New Method of Two-Dimensional Aerodynamic Design," Aeronautical Research Council, Repts. and Memoranda No. 2122, London, 1945.

[7]Zannetti, L., and Pandolfi, M., "Inverse Design Techniques for Cascades," NASA CR 3836, 1984.

[8]Volpe, G., "Geometric and Surface Pressure Restrictions in Airfoil Design," AGARD Rept. 780, June 1990.

[9]Iollo, A., Ferlauto, M., and Zannetti, L., "An Aerodynamic Optimization Method Based on the Inverse Problem Adjoint Equations," *Journal of Computational Physics*, Vol. 173, 2001, pp. 87–115.

[10]Darmofal, D., Moinier, P., and Giles, M., "Eigenmode Analysis of Boundary Conditions for the One-Dimensional Preconditioned Euler Equations," *Journal of Computational Physics*, Vol. 160, No. 1, 2000, pp. 369–384.

[11]Pandolfi, M., "Contribution to the Numerical Prediction of Unsteady Flows," *AIAA Journal*, Vol. 22, 1983, pp. 37–46.

[12]Osher, S., and Salomon, F., "Upwind Difference Schemes for Hyperbolic Systems of Conservation Laws," *Mathematics of Computation*, Vol. 38, 1982, pp. 339–374.

[13]Ferlauto, M., Iollo, A., and Zannetti, L., "Fan and Propeller Design via Inverse Problem Adjoint Equations," International Symposium on Air Breathing Engines, ISABE Paper 2001-1160, Sept. 2001.

[14]Ferlauto, M., Iollo, A., and Zannetti, L., "Coupling of Inverse Methods and Optimization Techniques for Aerodinamic Shape Design," AIAA Paper 2000-0668, Jan. 2000.

[15]Bena, C., Larocca, F., and Zannetti, L., "Design of Multistage Axial Flow Turbines and Compressors," IMech-E 3rd European Conf. on Turbomachinery, Paper C557/047/99, March 1999.

[16]Harten, A., Engquist, B., and Osher, S., "Uniformly High-Order Accurate Essentially Non-Oscillatory Schemes III," *Journal of Computational Physics*, Vol. 71, 1987, pp. 231–303.

[17]Fletcher, R., *Practical Methods of Optimization*, Wiley, New York, 1980.

[18]Jameson, A., "Aerodynamic Design via Control Theory," *Journal of Scientific Computing*, Vol. 3, 1988, pp. 233–260.

[19]Jameson, A., Martinelli, L., and Pierce, N. A., "Optimum Aerodynamic Design using the Navier–Stokes Equations," *Theorethical and Computational Fluid Dynamics*, Vol. 10, 1998, pp. 213–237.

[20]Iollo, A., and Salas, M., "Contribution to the Optimal Shape Design of 2D Internal Flows with Embedded Shocks," *Journal of Computational Physics*, Vol. 125, 1996, pp. 124–134.

K. Fujii
Associate Editor